

# 1 **Monitoring European anthropogenic NO<sub>x</sub> emissions from space**

2 Ronald J. van der A<sup>1\*</sup>, Jieying Ding<sup>1\*</sup>, Henk Eskes<sup>1</sup>

3 <sup>1</sup>Royal Netherlands Meteorological Institute (KNMI), De Bilt, The Netherlands

4

5 \*Corresponding authors: Ronald van der A (avander@knmi.nl), Jieying Ding (jieying.ding@knmi.nl)

6

## 7 **Abstract**

8 Since the launch of TROPOMI on the S5p satellite, NO<sub>2</sub> observations have become available  
9 with a resolution of 3.5x5 km, which makes monitoring NO<sub>x</sub> emissions possible at the scale of  
10 city districts and industrial facilities. For Europe, emissions are reported on an annual basis for  
11 country totals and large industrial facilities and made publicly available via the European  
12 Environmental Agency (EEA). Satellite observations can provide independent and more timely  
13 information on NO<sub>x</sub> emissions. A new version of the inversion algorithm DECSO (Daily  
14 Emissions Constraint by Satellite Observations) has been developed for deriving emissions for  
15 Europe on a daily basis, averaged to monthly mean maps. The estimated precision of these  
16 monthly emissions is about 25% for individual grid cells. These satellite-derived emissions  
17 from DECSO have been compared to the officially reported European emissions and spatial-  
18 temporal disaggregated emission inventories. The country total DECSO NO<sub>x</sub> emissions are  
19 close to the reported emissions and the emissions compiled by the Copernicus Atmospheric  
20 Monitoring Service (CAMS). The comparison of the spatial distributed NO<sub>x</sub> emissions of DECSO  
21 and CAMS showed that the satellite-derived emissions are often higher in cities, while similar  
22 for large power plants and slightly lower in rural areas.

23

24

## 25 **1. Introduction**

26 Nitrogen oxides (NO<sub>x</sub>) concentrations play an important role in air quality, the nitrogen cycle,  
27 and as precursor for climate gasses, knowledge of NO<sub>x</sub> emissions is also important for climate  
28 studies (Shindell et al., 2005). Because of the importance of NO<sub>x</sub> for air quality, in Europe both  
29 the concentrations in air and emissions to air are regulated. Country total NO<sub>x</sub> emissions need  
30 to be reported by EU countries as part of the Convention for Long-Range Transboundary Air  
31 Pollution (LRTAP, Pinterits et al., 2021) and the National Emission reductions Commitments  
32 (NEC) Directive (NEC, 2023) of the European Union. More detailed emission inventories

33 including spatial distribution are compiled based on reported emissions, statistical  
34 information (e.g. population density) and activity data. Examples of these inventories on a  
35 global scale are the Emissions Database for Global Atmospheric Research (EDGAR, EC-JRC/PBL,  
36 2011, Janssens-Maenhout et al., 2015) and the various global and regional emission  
37 inventories developed in the context of the Copernicus Atmosphere Monitoring Service  
38 (CAMS, Innes et al, 2019) of the EU Copernicus programme. These gridded emission  
39 inventories are widely used for global atmospheric composition and regional air quality  
40 modelling. The realism of the air quality model results depends largely on the accuracy of the  
41 emission inventory (Thunis et al, 2021).

42 Since the availability of satellites capable of measuring NO<sub>2</sub> concentrations in the atmosphere,  
43 methods have been developed to derive top-down emissions (Streets et al., 2013). These top-  
44 down emissions have the major advantage that they are based on observations. This fully  
45 independent source of information provides the possibility to check reported emissions,  
46 monitor rapid changes (e.g. due to the COVID-19 lockdowns) and has the potential of finding  
47 unknown and unreported sources. Polar-orbiting satellites with a global daily coverage within  
48 1-3 days, allow monitoring of changes in emissions on timescales of days to weeks. Nadir-  
49 viewing satellites measure total column concentrations of trace gases, and the distinction of  
50 source sector type must be deduced via the source location. A popular inversion technique  
51 for NO<sub>x</sub> emissions is the divergence method of Beirle et al. (2021, 2023), where the average  
52 flux is calculated in grid cells, assuming local mass balance, to find the sources of the  
53 emissions. Although no model is needed in this method, the required spatial derivations lead  
54 to noisy fields for daily overpasses, and it only provides useful emissions when averaged over  
55 a longer period. Furthermore, assumptions must be made for the chemical lifetime, and  
56 simplifications lead to biases, especially in background emissions. A second class of methods  
57 is based on plume fitting (Fioletov et al., 2022). This method can be applied to individual  
58 overpasses but needs well-defined plume shapes which is not trivial for areas with multiple  
59 sources close together. Both these methods simplify atmospheric transport as two-  
60 dimensional. For a full three-dimensional description of transport and chemistry, a data  
61 assimilation or inverse modelling method is used to match the model results and observations  
62 by adapting the emissions (Miyazaki et al., 2017, Fortems-Cheiney et al., 2021). A typical  
63 application of satellite-derived emissions is the study of the impact of recent events, for  
64 example the effect of COVID regulations (Ding et al., 2020). Top-down emissions are also used

65 for the verification and support to improve current emission inventories (Guevara et al., 2021;  
66 Crippa et al., 2023). Guevara et al. (2021) and Crippa et al. (2023) concluded that interesting  
67 aspects for future studies are the spatial distribution, seasonal time profiles and multi-annual  
68 trends of the emissions.

69 In this study we present the latest version 6.3 of the Daily Emissions Constrained by Satellite  
70 Observations DECSO (DECSO) inversion algorithm. The DECSO algorithm can be applied for  
71 the operational monthly (or even daily) monitoring of emissions for any region worldwide  
72 based on satellite observations of trace gases such as SO<sub>2</sub>, NH<sub>3</sub> or NO<sub>2</sub>. In this paper this new  
73 DECSO version has been applied to NO<sub>2</sub> observations over Europe from the TROPOMI  
74 instrument (Veefkind et al., 2012) on board the Sentinel-5P satellite. The DECSO system is  
75 efficient, requires only a single forward run of the chemistry-transport model and takes about  
76 12 hours to process one month of data on a 30-core computer. Here, we will evaluate the  
77 performance of DECSO on various spatial scales (from national to point sources) by  
78 comparison with the various bottom-up emission inventories available for Europe. By  
79 comparing satellite derived emissions with bottom-up emissions we gain insight in the  
80 accuracy of both derived emission datasets.

81

82

## 83 **2. Methodology and data**

84

### 85 **2.1 DECSO: inversion of TROPOMI observations**

86 The inversion algorithm DECSO (Daily Emissions Constrained by Satellite Observations) has  
87 been developed at KNMI for the purpose of deriving emissions for short-lived gases (Mijling  
88 and van der A, 2012). DECSO is using a Kalman Filter implementation for assimilating  
89 emissions. The emission forecast model is based on persistency from the analysis, while the  
90 concentrations are calculated from the emissions by a chemical transfer model (CTM) and  
91 compared to satellite observations. The sensitivity of concentrations to emissions is calculated  
92 from multiple forward trajectories to account for the transport of the short-lived gas, but only  
93 a single CTM forward run is needed. More detailed information on the method can be found  
94 in Mijling and Van der A (2012), the validation is described in Ding et al. (2017a) and the  
95 previous latest published version, i.e. DECSO v5.2, is described in Ding et al. (2020). Recent  
96 developments of the algorithm to improve its resolution and quality have led to the release

97 of version 6.3. The most important updates are the use of a recent version of the chemical  
98 transport model, improved use of TROPOMI observations and changes in the sensitivity matrix  
99 calculations. More details of these updates follow below.

100 The chemical transport model in DECSO has been upgraded to the latest version of the  
101 Eulerian regional off-line CTM CHIMERE v2020r3 (Menut et al., 2021). The implementation of  
102 CHIMERE in DECSO was described in Ding et al. (2017b). In this study CHIMERE is combined  
103 with the Copernicus Landcover 2019 data (Buchhorn et al., 2020) and HTAP v3 (Hemispheric  
104 Transport of Air Pollution, Crippa et al., 2023) of 2018 for the source sector split of the  
105 emissions. The meteorological input data for CHIMERE are the operational European Centre  
106 for Medium-Range Weather Forecasts (ECMWF) weather forecasts.

107 The sensitivity matrix, giving the relationship between emissions and concentrations, is based  
108 on trajectories calculated with a high temporal resolution (a time step of 7.5 minutes). In the  
109 new version the relationship between emissions and concentrations is limited to a maximum  
110 distance of 150 km to avoid effects of errors in the trajectories over longer distances. With  
111 this sensitivity matrix not only observations over the source are affecting the derived  
112 emissions, but also the transported concentrations away from the source within 150 km. The  
113 default settings of DECSO described here are for a grid resolution of 0.2 degree. For higher  
114 grid resolutions, the settings for temporal resolution and maximum trajectory distance are  
115 increased and reduced respectively.

116 The error parametrizations for the emission model and observations are based on the  
117 Observation-minus-Forecast (OmF) and the Observation-minus-Analysis (OmA) statistics of  
118 previous runs. The latest version of DECSO can also be applied to simultaneous optimisation  
119 of emissions of NO<sub>x</sub> and NH<sub>3</sub> (Ding et al., 2024).

120 Although HTAP v3 has been used for the sector distribution of emissions and other species in  
121 CHIMERE, no use is made of a -priori (bottom-up) NO<sub>x</sub> emissions in DECSO. DECSO is using a  
122 persistency forward model in which the emissions of the current day are equal to the  
123 emissions of the previous day. In addition, there is a strong dependency of the calculated  
124 emissions on the observations as shown in Ding et al. (2021). Since the derived emissions are  
125 updated by addition and not by multiplication factors, unknown sources or emission changes  
126 are detected fast.

127 TROPOMI is a spectrometer instrument onboard the Sentinel 5P satellite, which was launched  
128 in October 2017 and is flying a sun-synchronous polar orbit with a local overpass time of 13:30.

129 The measured NO<sub>2</sub> columns are derived from the visible band that has a spectral resolution  
130 of 0.54 nm (0.2nm sampling) and a signal-to-noise ratio of about 1500 (van Geffen et al.,  
131 2022a). The NO<sub>2</sub> tropospheric columns have a spatial resolution of 5.5 x 7 km (5.5 x 3.5 km  
132 since 6 August 2019) over a swath of about 2600 km, which means that global coverage is  
133 reached daily.

134 We are using the latest version 2.4 reprocessed and offline TROPOMI NO<sub>2</sub> observations (van  
135 Geffen et al.,2022b) converted to super-observations as described in Ding et al. (2020). The  
136 modelling of NO<sub>2</sub> in the free troposphere, governed by processes like lightning, deep  
137 convection, aircraft emissions or long-range transport, is often simplified in regional air-quality  
138 models focusing on surface concentrations. However, the TROPOMI NO<sub>2</sub> product is providing  
139 a tropospheric column, which includes the Planetary Boundary Layer (PBL) and the free  
140 troposphere. As a result, model biases in the free troposphere may be a significant source of  
141 systematic error in the model-satellite comparisons (Douros et al., 2023). To mitigate this  
142 problem we adapt the TROPOMI NO<sub>2</sub> retrieval by replacing the tropopause level by a 700 hPa  
143 level. The stratosphere + free troposphere NO<sub>2</sub> column from the TM5-MP (Tracer Model 5,  
144 <https://tm5.site.pro/>, Williams et al., 2017) assimilation system are now subtracted from the  
145 satellite-observed total column, and new retrieved layer column amounts, air-mass factors  
146 and kernels are computed for the surface to 700 hPa layer in the same way as they are  
147 computed for the tropospheric column (van Geffen et al., 2022b). The observations with a  
148 cloud radiance fraction of more than 50% (this corresponds to a cloud fraction of about 20%)  
149 have not been used. For Europe, it means that about 45% of the observations are used.

150 Superobservations (Sekiya et al., 2022) are constructed as the area-weighted mean of cloud-  
151 free (qa value > 0.75) TROPOMI observations over the CHIMERE model grid cells. For a grid of  
152 0.2x0.2 degree a superobservation contains about 10 to 15 TROPOMI NO<sub>2</sub> observations. The  
153 use of superobservations improves the signal-to-noise ratio and it reduces the calculation time  
154 of DECSO. On the other hand, the sampling of transported NO<sub>2</sub> from the observations  
155 calculated back to the source on the emission grid, based on superobservations, will slightly  
156 spread out the derived emissions and reduce their spatial resolution compared to using  
157 individual observations. The chosen size of the superobservation grid of 0.2x0.2 degree is  
158 therefore a compromise between noise, calculation speed and spatial resolution. Knowing  
159 that the smoothing of emissions after averaging can be imagined as a distribution by a pyramid  
160 shape weighting function around a point source, a deconvolution is possible for isolated

161 emission sources with a known location. The current version of DECSO makes use of the  
162 superobservations software as also used in Sekiya et al. 2022. The software has been further  
163 developed focusing on a realistic description of the superobservation uncertainty (Rijsdijk et  
164 al, 2024) and this new superobservation software is planned to be used in future DECSO  
165 studies.

166 In a post-processing step, the total monthly NO<sub>x</sub> emissions are split into anthropogenic and  
167 (biogenic) soil emission contributions Lin et al. (2023). The soil emissions show a strong  
168 seasonal cycle with low emissions in winter, while the anthropogenic emissions are more  
169 constant over the year. The soil NO<sub>x</sub> emissions are derived by fitting the monthly emissions in  
170 a selection of grid-cells without any significant anthropogenic contribution according to land-  
171 use data. In this way the monthly averaged soil NO<sub>x</sub> emissions in the categories for forest,  
172 agricultural and shrub-land are derived. These monthly soil NO<sub>x</sub> emissions are weighted with  
173 the land-use type of these 3 categories in each grid cell and subtracted from the total derived  
174 NO<sub>x</sub> emissions to end up with the anthropogenic NO<sub>x</sub> emissions discussed in this study. This  
175 splitting method is described in detail in Lin et al. (2023).

176 For the monthly emissions also the precision of the emission in each grid cell has been  
177 calculated. Each daily NO<sub>x</sub> emission per grid cell derived by DECSO is accompanied by a  
178 standard deviation calculated according the Kalman Filter equations (the standard deviation  
179 is part of the emission data product of DECSO). As the starting point of each daily step in the  
180 calculation by DECSO is the emissions of the previous day, the resulting emissions will show  
181 an autocorrelation in their errors. For each grid cell the autocorrelation function  $\rho_k$  (for time  
182 lag  $k$ ) has been calculated for each month. We see typically that the autocorrelation effects in  
183 the errors have disappeared completely after about 1 week.

184 When calculating the variance of the monthly mean values, we must take this autocorrelation  
185 function into account. The variance  $S$  of the monthly mean NO<sub>x</sub> emissions per grid cell is  
186 calculated following Bayley and Hammersley (1946) or Box et al. (2008) as

187

$$188 \quad S = \frac{\sigma^2}{n} \left[ 1 + 2 \sum_{k=1}^{n-1} \left( 1 - \frac{k}{n} \right) \rho_k \right] ,$$

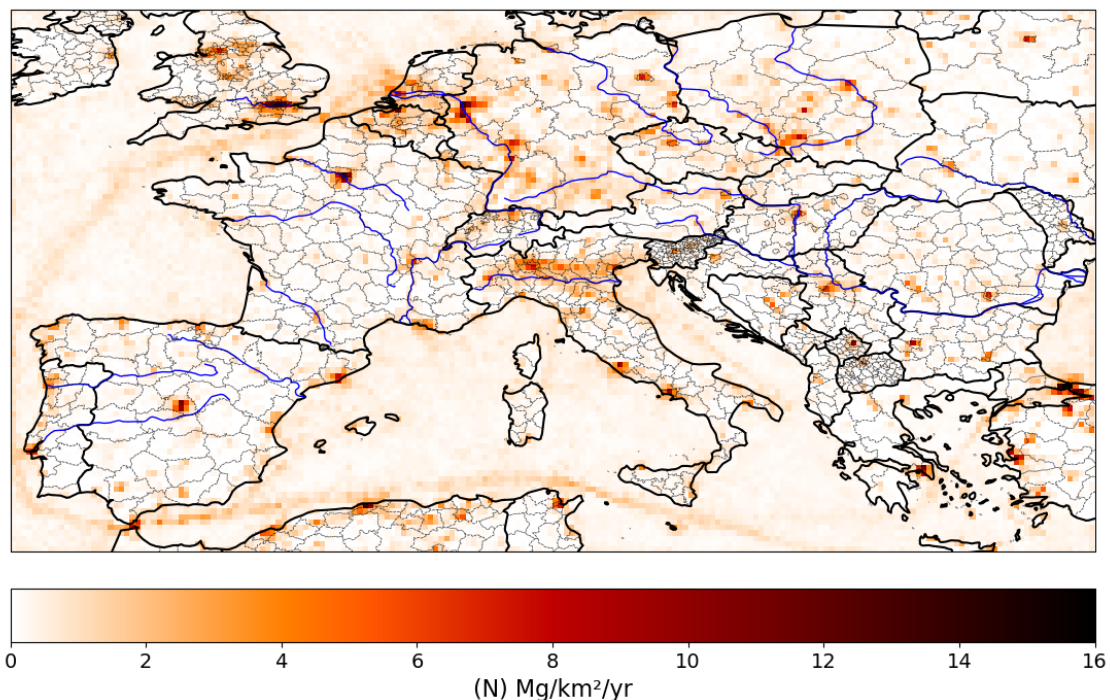
189

190 where  $\sigma$  is the mean standard deviation of the emissions over the month and  $n$  is the number  
191 of days in the month. We assume here that  $\sigma$  is not varying a lot over the month. This precision

192  $\sigma$  is calculated in the Kalman equations of the inverse modelling and it depends on the  
193 precision of the TROPOMI NO<sub>2</sub> superobservations. The precision depends on the location and  
194 emission magnitude, but on average the precision is estimated as 8% for annual emissions,  
195 25% for monthly emissions and between 10 and 60 % for the daily emissions.

196  
197 In this study we will focus only on NO<sub>x</sub> emissions. Although DECSO has been applied to many  
198 regions in the world, we will show results for a domain over Europe (35°-55°N, 10°W-30°E) and  
199 for 0.2 degree spatial resolution. The temporal resolution of our inversion is daily, usually  
200 averaged to monthly or yearly mean values, for the period of 2019 to 2022. Figure 1 shows  
201 the average annual emissions for 2019 as derived with DECSO version 6.3. In the Figure the  
202 emissions of major cities and industrial facilities can be identified. Ship emissions show up  
203 clearly in most seas where many ships follow the same route. Other areas over sea appear  
204 noisier since ship locations are moving while emitting NO<sub>x</sub>. The most polluted regions in  
205 Europe are the densely populated and industrial regions in the Po Valley, the Ruhr area, and  
206 the West of the Netherlands.

207



208

209 **Figure 1** The annual-averaged anthropogenic NO<sub>x</sub> emissions for 2019 derived from  
210 TROPOMI NO<sub>2</sub> observations using the DECSO algorithm.

211

212

## 213 **2.2 Databases for validation**

214 For comparison of the emission results in Europe we will use several inventories, all based on  
215 official emissions reported to the European Environmental Agency (EEA). The first one is the  
216 inventory of national emissions per source category reported under the National Emission  
217 reductions Commitments (NEC) Directive of the European Union. Another similar inventory is  
218 the Emission inventory reported under the Convention on Long-range Transboundary Air  
219 Pollution (LRTAP), which give the country totals of emissions in various source categories. The  
220 last one we will use is the European Pollutant Release and Transfer Register (E-PRTR; EPTR, 2012),  
221 which is a database of the individual emissions of the biggest industrial facilities (above  
222 0.1Mg/year) in Europe. The E-PRTR emissions data are reported on an annual basis. From here  
223 on we will call those databases simply NEC, LRTAP and E-PRTR. Besides comparison with these  
224 officially reported emissions, we will also compare our emissions to the regional  
225 anthropogenic emission inventory CAMS-REG-ANT v5.1 for air quality in Europe (Kuenen et  
226 al., 2022) developed for the Copernicus Atmospheric Monitoring Service (CAMS), hereafter  
227 called CAMS-REG. For these annual CAMS-REG emissions we use the total emissions regridded  
228 from  $0.1^\circ \times 0.05^\circ$  to  $0.2^\circ \times 0.2^\circ$  and exclude the soil emissions (i.e. agricultural categories), since  
229 soil emissions are also excluded in DECSO. Temporal profiles are also derived in CAMS, which  
230 allow us to compare timeseries for monthly averaged values. We will use the Copernicus  
231 Atmosphere Monitoring Service TEMPORal profiles (CAMS-GLOB-TEMPO, Guevara et al.,  
232 2021,2023) for comparison of monthly variations in anthropogenic  $\text{NO}_x$  emissions. The global  
233 emission data version 5.3, called CAMS-GLOB-TEMPO, on a resolution of  $0.1^\circ \times 0.1^\circ$  has been  
234 regridded to  $0.2^\circ \times 0.2^\circ$  resolution and is hereafter referred to as CAMS-TEMPO.

235

## 236 **3. Evaluation of the satellite derived emissions**

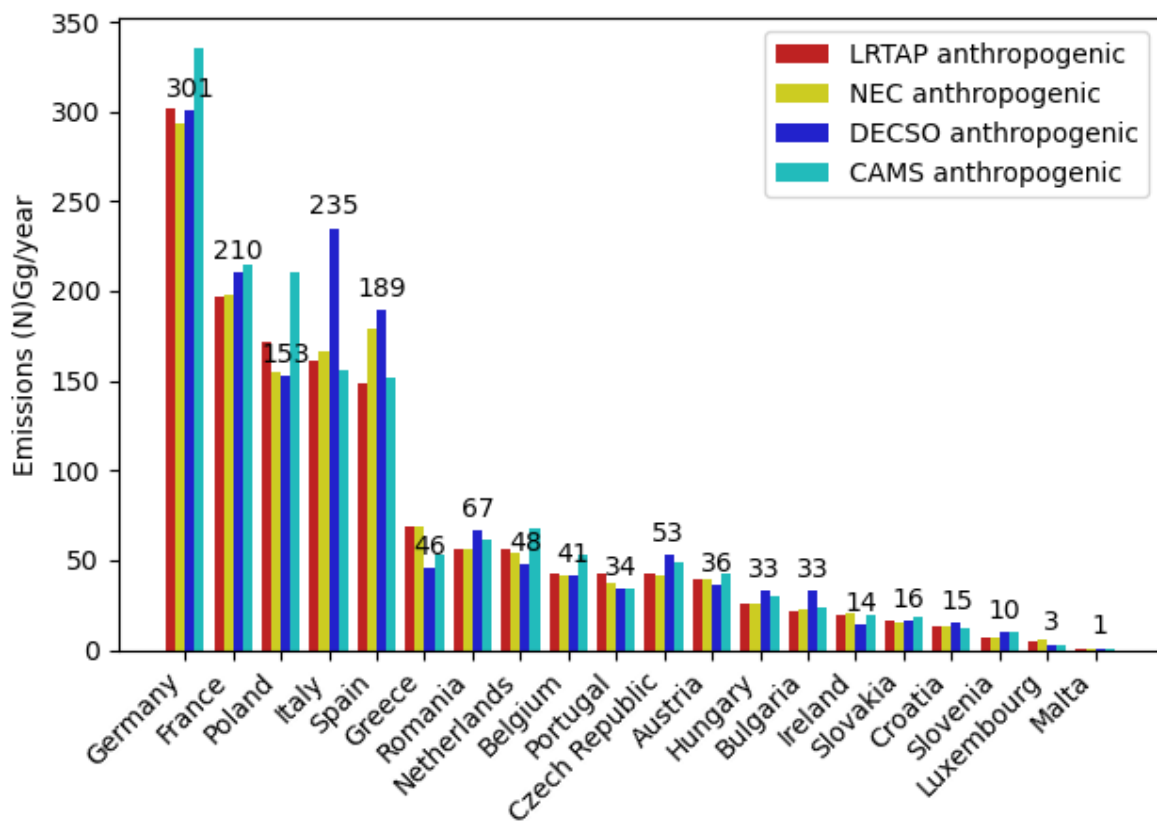
237

### 238 **3.1 Country scale intercomparison**

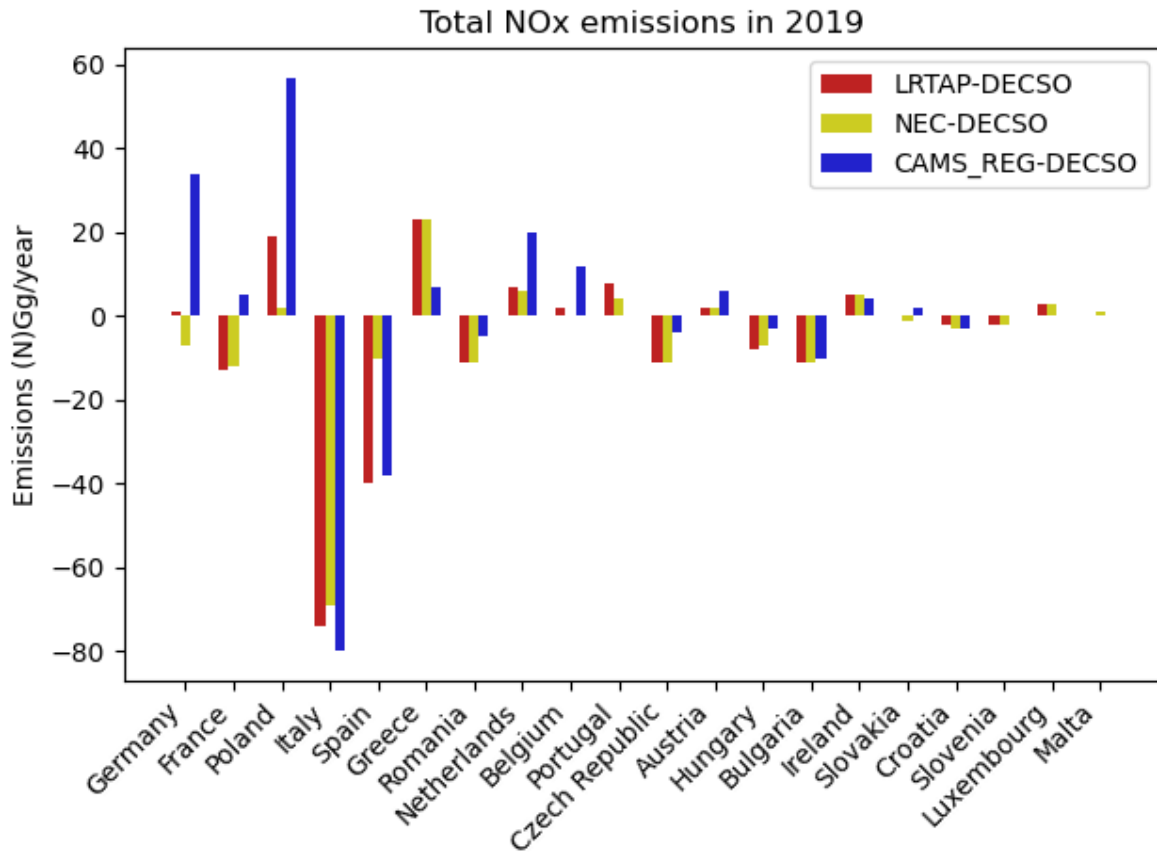
239 The  $\text{NO}_x$  emissions derived with DECSO have been summed over the countries in our domain  
240 and compared to the registered total emissions in NEC and LRTAP. Note that for the national  
241 total emissions the spatial resolution or spatial smoothing of the derived emissions play hardly  
242 any role. In total 21 countries are completely covered by our geographical domain and have  
243 reported their emissions. The total anthropogenic emissions (excluding soil emissions) for all



244 these 21 countries are 1.44 Tg/year according both LRTAP and NEC. The total calculated  
 245 anthropogenic emissions by DECSO are 1.54 Tg/year, about 7% higher than the reported  
 246 emissions. The total anthropogenic emissions of CAMS-REG (excluding soil emissions) for the  
 247 same region are 1.54 Tg/year, in agreement with DECSO. Note that the total soil emissions  
 248 derived by DECSO are 0.78 Tg/yr for the same region, but this number cannot be compared  
 249 because soil emissions in LRTAP and NEC are only given for the agricultural sector and not for  
 250 forestry. The anthropogenic country totals are shown in Figure 2. In general, we see a good  
 251 agreement with the official reported country total emissions of LRTAP and NEC except for Italy,  
 252 which has much lower reported emissions. Greece, on the other hand, has higher registered  
 253 emissions, but the mismatch might be related to the difficult counting over the Greek islands,  
 254 since we have weighted the emissions by the land fraction in each grid cells to exclude  
 255 maritime emissions in these country totals. For CAMS-REG we see bigger deviations not only  
 256 for Italy, but also for Germany, Poland, and Spain. Note that Ireland is only partly in our  
 257 geographical domain and has therefore lower emissions according to DECSO. Besides the  
 258 comparison on a national level also on a provincial scale good agreement is found, as has been  
 259 shown for Catalonia in the EC-project SEEDS.  
 260



261



262

263 **Figure 2** (a) Country totals of anthropogenic NO<sub>x</sub> emissions (in (N)Gg/year) in the year  
 264 2019 according to databases LRTAP, NEC, CAMS-REG and the DECSO calculations. (b)  
 265 Differences in total emissions calculated by LRTAP, NEC, CAMS-REG compared to DECSO.

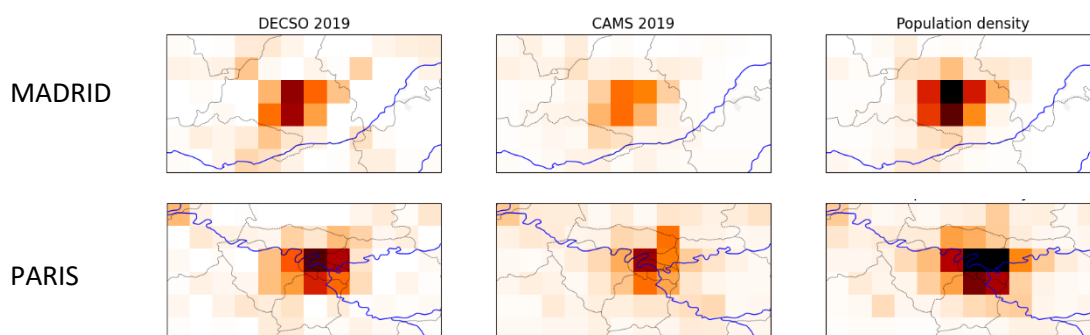
266

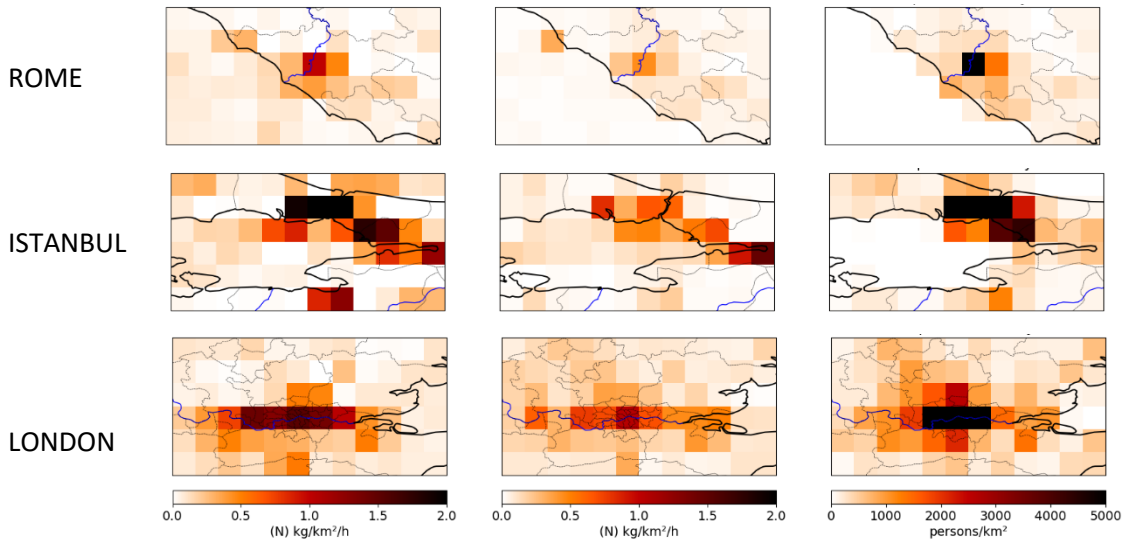
267

### 268 3.2 City scale

269 With our current spatial resolution of 0.2x0.2 degree, we observe emissions per city district  
 270 for large cities, but the geographical distribution can be slightly blurred by the 0.2 degree  
 271 resolution of the TROPOMI superobservations. Figure 3 shows the spatial distribution of the  
 272 annual emissions of DECSO and CAMS-REG for three of the largest cities in Europe: Madrid,  
 273 Paris, and Rome. Although DECSO show similar emissions for the country totals, we see that  
 274 for large cities DECSO estimates higher emissions in the city center, and more activities are  
 275 seen in the region surrounding the city, as compared to the CAMS-REG emissions. The  
 276 industrial complexes at Rouen located north-west of Paris, and at the port of Civitavecchia  
 277 located west of Rome are similar in DECSO compared to CAMS-REG. The area of Rouen used  
 278 to have an active oil refinery, but in recent years the industrial emissions are about 0.11

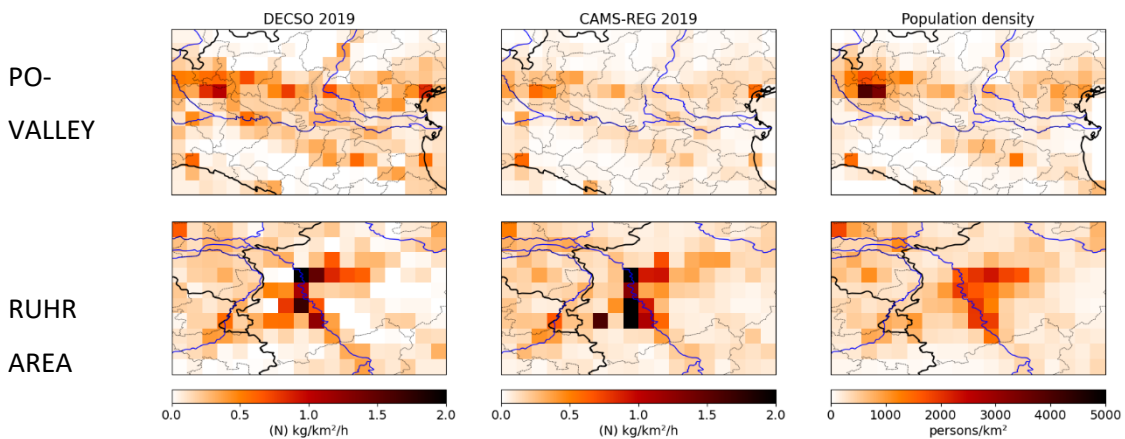
279 (N)kg/km<sup>2</sup>/h according to the E-PRTR database, which compares well to CAMS-REG and  
 280 DECSO. The spatial extent of high emissions in the Rome area is smaller in CAMS-REG, which  
 281 follows more the population density. However, the densely populated center of Rome is  
 282 surrounded by a busy ring road with a 20 km radius and a lot of commercial activities around  
 283 the city, which are not reflected in the population density map. The two powerplants at  
 284 Civitavecchia have reported emissions according to the E-PRTR database, which are equivalent  
 285 to about 0.17 (N)kg/km<sup>2</sup>/h per grid cell, which is closer to the DECSO derived emissions.  
 286 Although this study focuses mainly on the land emissions, we see in the map for Rome, that  
 287 the maritime emissions of CAMS-REG and DECSO disagree a lot, and this is a topic for further  
 288 studies. The city emissions in Istanbul are much higher in DECSO than in CAMS-REG. These  
 289 emissions will include a lot of ship emissions since it includes the busy ship route through the  
 290 Bosphorus Strait. The map of the greater area of London shows that DECSO has higher  
 291 emissions in the city, but lower outside the city. This is a pattern we see in general: in most big  
 292 cities the emissions derived by DECSO show a similar pattern than in CAMS-REG but the  
 293 emissions are higher, the emissions in rural regions on the other hand are usually lower in  
 294 DECSO than in CAMS-REG. The lower emissions in the rural regions can be seen in Figure S1,  
 295 which show maps for Europe of both emission products.  
 296 In Figure 3b we show the emission for two large industrial areas in Europe; the Po-Valley and  
 297 the Ruhr area. For the Po Valley the patterns are similar, but again the DECSO emissions are  
 298 higher in every city except for Genua in the Southeast corner of the map. For the Ruhr area,  
 299 the difference of emissions over the cities is small, the biggest differences are located at the  
 300 big power plants of Weisweiller, Neurath and Niederaussem around the open-pit lignite mine  
 301 of Hambach (the largest of Europe). The DECSO emissions are lower than CAMS-REG at the  
 302 locations of these power plants.  
 303





304 **Figure 3a** Zoom-in plots for 5 large cities in Europe to illustrate the differences in  
 305 distribution of emissions of DECSO (first column), CAMS-REG (second column) and the  
 306 population density (third column) per km<sup>2</sup>.

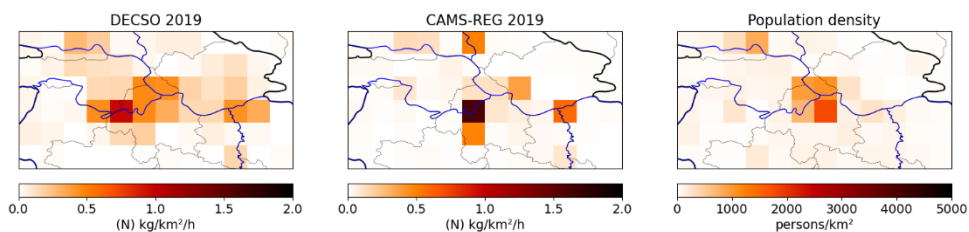
307



308

309 **Figure 3b** Zoom-in plots for two large densely populated and industrial regions in  
 310 Europe to illustrate the differences in distribution of emissions of DECSO (first column),  
 311 CAMS-REG (second column) and the population density (third column) per km<sup>2</sup>.

312

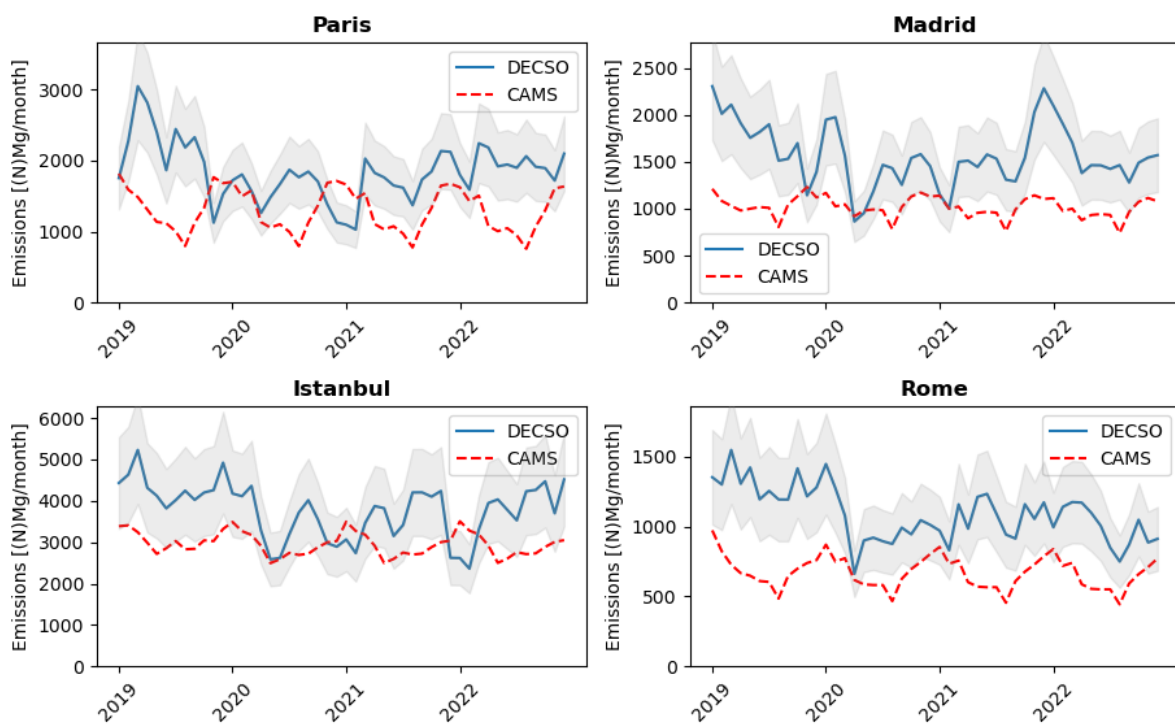


313

314 **Figure 3c** A map of North Serbia with  $\text{NO}_x$  emissions of DECSO, and CAMS-REG. The  
 315 population map shows especially the higher population for Belgrade. The emissions in DECSO  
 316 are mainly correlated with the locations of several coal power plants (Nikola Tesla -A, -B, and  
 317 -Kolubara) and a cement factory (Lafarge in Beocin) in the North-West.

318  
 319 On a European scale the biggest difference between CAMS-REG and DECSO was found for the  
 320 region around Belgrade in Serbia (Figure 3c). The city of Belgrade is identified by the higher  
 321 population density in Figure 3c. West of the city, the Nicola Tesla power plants are located,  
 322 which are strong emitters according to the E-PRTR database. They show up as a strong  
 323 emission source in the DECSO emissions, but they are mislocated in the current CAMS-REG  
 324 emissions.

325



326  
 327 **Figure 4** Timeseries of monthly  $\text{NO}_x$  emissions derived by DECSO for the cities Paris,  
 328 Madrid, Istanbul and Rome in the period 2019 to 2022. The shaded grey area shows the  
 329 estimated uncertainty on the DECSO emissions. The dotted red line shows the CAMS-TEMPO  
 330  $\text{NO}_x$  emissions for the same grid boxes.

331  
 332 Figure 4 shows examples of timeseries for city emissions, in this case for the cities of Paris,  
 333 Madrid, Istanbul and Rome (also shown in Figure 3a). In these plots we report the total

334 emissions in a square area of 5 by 5 grid cells centred on the city centre to make sure the  
335 whole city has been captured. As we had seen earlier, the DECSO emissions are on average  
336 higher than for CAMS-TEMPO, but also the seasonal cycle is different. The NO<sub>x</sub> emissions of  
337 CAMS-TEMPO show a seasonal cycle, which is almost identical each year, while DECSO show  
338 larger variations from year-to-year. We see clearly the effect of COVID regulations in all cities,  
339 that started first in March/April 2020 in Europe, and in the winter of 2020-2021 when strict  
340 COVID regulations were again in place. The general overall trend in this 4 year time period  
341 varies from city to city, but most cities show a slightly decreasing trend, partly related to a  
342 gradual decrease of emissions from road vehicles linked to European regulations.

343

### 344 **3.3 Intercomparison for large point sources**

345 To evaluate the performance of monitoring emissions from large point sources (LPS), we  
346 compare the DECSO emissions with emissions registered in the E-PRTR data base. The isolated  
347 LPS in Europe we selected are all large power plants close to lignite mines. Emissions from  
348 DECSO are slightly spread to adjacent grid cells because the spatial resolution of the emission  
349 field is less than the sampling of the grid cells as discussed in Sect. 2. To correct for this, we  
350 can deconvolute the emissions around the isolated point source, but here we choose to sum  
351 the anthropogenic emissions in the 3x3 grid cells including and around the point source to  
352 make sure all emissions are accounted for. For the four cases discussed below, no significant  
353 other sources exist in these 3x3 grid cell boxes, and soil emissions are excluded. The rural  
354 anthropogenic emissions in such an area of 3x3 grid cells in Europe we estimate as about 0.13  
355 (N)Gg/year by averaging the emissions of several similar rural 3x3 regions in Europe. We did  
356 not correct for this background signal, but we included this in the error bars of Figure 5

357 The first case is that of the Maritsa Iztok facility in Bulgaria located next to an open coal mine.  
358 There is no big city or any other industrial facility in the neighbourhood, except for the three  
359 big power plants of the Maritsa Iztok facility. Figure 5 shows the monthly averaged emissions  
360 calculated by the DECSO algorithm, the CAMS-TEMPO inventory, and the annual emissions  
361 from the E-PRTR database for the Maritsa facility. For a fair comparison we selected for CAMS-  
362 TEMPO also the same 3x3 grid cells around the LPS. For the period 2019-2022 the annual  
363 emissions are given in Table 1 according to DECSO, CAMS-TEMPO and E-PRTR. The difference  
364 in annual emissions between DECSO, CAMS-TEMPO and E-PRTR of the Maritsa facility are  
365 within 20-40 %, although DECSO is the highest. The CAMS-TEMPO emissions show a negative

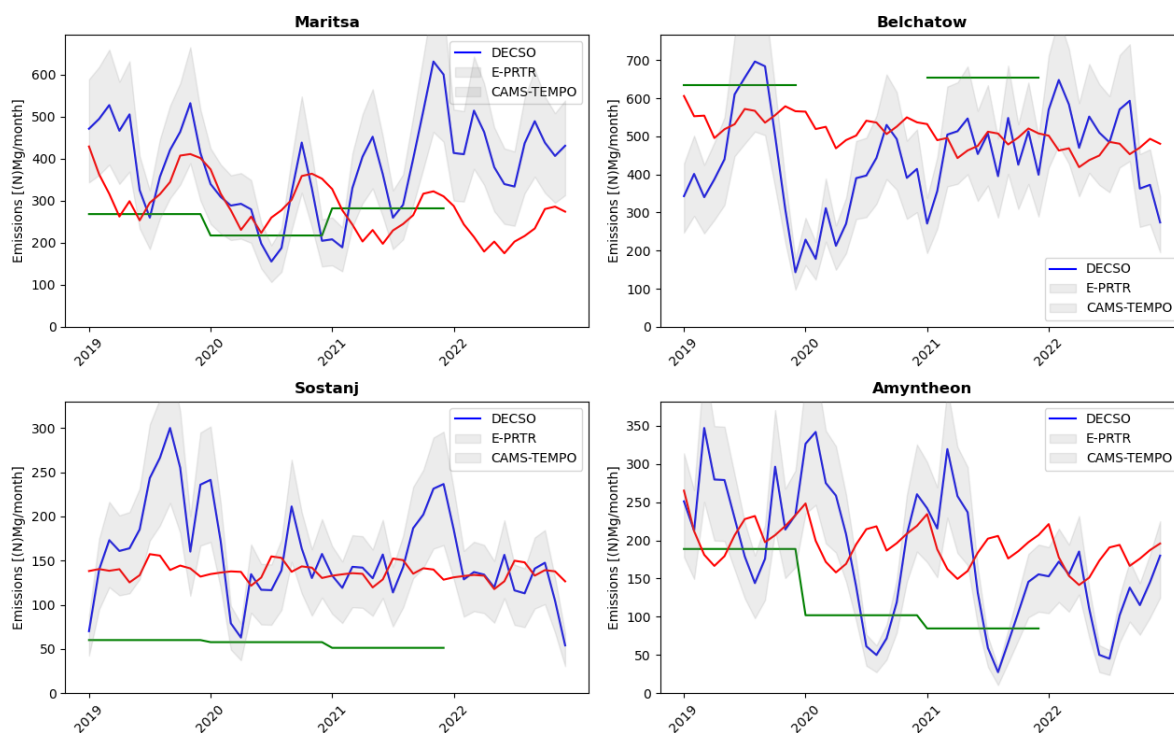
366 trend, which is not visible in DECSO that shows the highest emissions for 2022. Unfortunately,  
367 no E-PRTR data for 2022 is yet publicly available.

368 The second power plant is the Bełchatów power plant in Poland with its capacity of 5,053 MW,  
369 the biggest power plant of Europe. It is also one of the most polluting power plants in the  
370 world and gets its fuel from the adjacent lignite coal mine of Bełchatów (Guevara et al., 2023).  
371 For the year 2020 no emission values are reported in the current E-PRTR database. For the  
372 years 2019 and 2021 DECSO observes high emissions of about 5.5 Gg per year, but this is lower  
373 than the reported value of more than 7 Gg per year. CAMS-TEMPO also shows lower emissions  
374 with a negative trend. Godłowska et al. (2023) showed the stack measurements of this power  
375 plant in their Figure 7, which also are in general lower than the E-PRTR values.

376 The next selected isolated power plant is the Šoštanj lignite power plant in the Velenje basin  
377 in a mountainous area of Slovenia. It is responsible for one third of the electricity need of  
378 Slovenia (Boznar et al., 2012). For this LPS both CAMS-TEMPO and DECSO show more than  
379 two times higher emissions than E-PRTR, which is too large to be explained by the small cities  
380 or other small sources located in the neighbourhood.

381 The last case is that of the power plants of the Ptolemais-Amyntheon and Florina coal basins  
382 in West Macedonia, Greece, which were also studied by Skoulidou et al. (2021). There are 5  
383 power plants associated with and located at this basin, but only three are still active: Agios  
384 Dimitrios (1595 MW), Kardias (1200 MW), and Amyntheon (600 MW) (Kostakis, 2009). For  
385 2021 no data was reported for Amyntheon in the E-PRTR database. The reported values of the  
386 E-PRTR database match those of CAMS-TEMPO and DECSO quite well, except for the year 2020  
387 that marks the start of a decrease in emissions in this region. The decreasing trend can be  
388 seen in all three emissions time lines, but is strongest in the E-PRTR time series. Most notable  
389 in the Figure is the strong seasonal cycle in DECSO NO<sub>x</sub> emissions for the Greek power plants  
390 with the lowest emissions in summer time. This can be related to the availability of more  
391 sustainable energy sources in the summer months.

392



393  
 394 **Figure 5** Timeseries of the  $\text{NO}_x$  emissions of the selected LPS in Europe as estimated by  
 395 DECSO (blue line), E-PRTR (green line) and CAMS-TEMPO (red line). The shaded grey area  
 396 shows the estimated uncertainty on the DECSO emissions.

397  
 398 From this comparison for several large LPS in Europe, we see that CAMS-TEMPO and DECSO  
 399 are often larger than the reported emissions in E-PRTR. In view of the completely different  
 400 methodologies and the estimated precision of 25 % for DECSO monthly emissions, the annual  
 401 values of CAMS-TEMPO and DECSO are often in reasonable agreement (within 20%), but the  
 402 variability of DECSO is much higher than of CAMS-TEMPO. Emissions of thermal power plants  
 403 are more intermittent because of the variability of energy demand and variability in energy  
 404 supply introduced by solar and wind energy sources (Kubik et al., 2012). Note also that CAMS-  
 405 TEMPO has the exact same seasonal variability for each of the 4 years, which seems  
 406 unrealistic. The CAMS-TEMPO emissions in the period 2019 to 2022 show for most studied  
 407 LPS a constant negative trend, which was generally not detected in DECSO. Without additional  
 408 information it is difficult to draw any conclusions on the performance for LPS, but DECSO  
 409 supplies additional information on these industrial facilities in Europe and the largest  
 410 discrepancies may be caused by strong diurnal variability (while TROPOMI observes at about  
 411 13:30) and will be interesting for further investigation.



412 In all cases we see lower emissions in 2020 during the COVID-19 pandemic. In this period the  
 413 demand of energy was lower and while renewable energy output remained similar, the energy  
 414 from lignite-based power plants was in relatively less demand (Quitow et al., 2021).

415

416 **Table 1** Annual NO<sub>x</sub> emissions (N)Gg/year of the four lignite power plants. CAMS in  
 417 the table refers to CAMS-TEMPO.

Facility	2019			2020			2021			2022		
	CAMS	DECSO	E-PRTR	CAMS	DECSO	E-PRTR	CAMS	DECSO	E-PRTR	CAMS	DECSO	E-PRTR
	Unit: (N)Gg/yr			Unit: (N)Gg/yr			Unit: (N)Gg/yr			Unit: (N)Gg/yr		
Maritsa	4.1	5.2±0.4	3.2	3.6	3.3±0.3	2.6	3.2	4.6±0.4	3.4	2.8	5.0±0.4	-
Belchatow	6.6	5.5±0.4	7.6	6.3	4.3±0.3	-	5.9	5.4±0.4	7.9	5.6	6.0±0.5	-
Sostanj	1.7	2.4±0.2	0.69	1.7	1.7±0.1	0.66	1.6	1.9±0.2	0.62	1.5	1.3±0.1	-
Amyntheon	2.5	2.8±0.2	2.3	2.4	2.3±0.1	1.2	2.3	2.0±0.2	1.0	1.6	1.3±0.1	-

418

419

#### 420 4. Discussion

421 We presented the latest version of the DECSO algorithm, version 6.3. Updates has been made  
 422 for the superobservations, the chemical transport model, the sensitivity matrix and the error  
 423 parametrization. The new version also includes an error estimate for the monthly NO<sub>x</sub>  
 424 emission data taking into account the autocorrelation in time. The new DECSO version has  
 425 been applied to the domain of Europe and show more spatial details than before as a result  
 426 of the higher resolution of TROPOMI observations compared to earlier satellite observations.  
 427 In the comparison with CAMS-REG over Europe (where emissions are usually well-known) the  
 428 deviations are small (within 10%) when looking at country scale. For point sources the spread  
 429 in the differences is much higher, but no systematic effect is yet found. For cities DECSO show  
 430 higher emissions, while CAMS-REG is higher for rural regions. On a European scale the biggest  
 431 difference between CAMS-REG and DECSO was found for the region West of Belgrade in  
 432 Serbia, where the Nicola Tesla power plants are located. While these show up as a strong  
 433 emission source close to Belgrade in both the DECSO emissions and the E-PRTR database, they  
 434 are not included or mislocated in the CAMS-REG emissions. This is a prominent example that  
 435 demonstrates the value of monitoring emissions with satellite observations.

436 The precision of the derived emissions by DECSO are given for each grid cell in the data files.  
 437 In general, we can say that the precision of NO<sub>x</sub> emissions given per grid cell (0.2x0.2 degree)  
 438 is about 8% for annual emissions, 25% for monthly emissions and between 10 and 60 % for

439 the daily emissions. When averaging over a larger domain the precision will of course become  
440 higher by the square root of the number of grid cells.

441 The comparison between CAMS-REG and DECSO emissions showed that DECSO is very similar  
442 to CAMS-REG for the spatial distribution and the country totals. While compared to the  
443 reported emissions in NEC or LRTAP, DECSO is 7 % higher. Validation of the TROPOMI NO<sub>2</sub>  
444 observations showed that, when using averaging kernels, the bias of the tropospheric column  
445 is estimated as -8% on average by comparison with MAX-DOAS observations (Keppens and  
446 Lambert, 2023). This bias of -8% should result in lower emissions by DECSO and the deviation  
447 between DECSO and other inventories would be higher in reality. Keppens and Lambert (2023)  
448 further report that for polluted regions the mean bias of the TROPOMI NO<sub>2</sub> observations is  
449 stronger, about -29%, while for clean areas the median bias is positive and about +13% (when  
450 using averaging kernels). This would be contradictory to our findings over cities, where DECSO  
451 shows higher emissions than CAMS-REG. Another potential cause of biases in our emissions  
452 is the CHIMERE model. More research is needed for a better understanding of the validation  
453 results of TROPOMI observations, CHIMERE performance, and the comparisons between  
454 DECSO and CAMS.

455 This study shows the potential of DECSO for operational emission monitoring for Europe. The  
456 monitoring of LPS is only possible for isolated sources, thus a future improvement can be  
457 made by providing the emissions on a higher resolution at the cost of longer processing time.  
458 This will allow the study of more isolated LPS. DECSO has already demonstrated its  
459 performance on a 0.1°x0.1° for smaller regions like the Yangtze River Delta (Zhang et al.,  
460 2023), West Siberia (van der A et al., 2020) and the Netherlands.

461 In this study the focus was on Europe, but in other regions of the world emissions might be  
462 less well-known. For these regions DECSO can or has been applied since we have global  
463 satellite observations. Recently we have applied DECSO to areas in Africa, where several mines  
464 with high NO<sub>x</sub> emissions were found that were unreported in bottom-up emission inventories  
465 like EDGAR or CAMS. This shows the possibilities also for application of DECSO in the Global  
466 South.

467

468 **Data availability**

469 The TROPOMI NO<sub>2</sub> data version 2.4 are available via the Copernicus website  
470 <https://dataspace.copernicus.eu/> and via the TEMIS website  
471 <https://www.temis.nl/airpollution/no2.php> (<https://doi.org/10.5270/S5P-9bnp8q8>).  
472 The NO<sub>x</sub> emissions of DECSO v6.3 are available on the GlobEmission website:  
473 [https://www.temis.nl/emissions/region\\_europe/datapage\\_nox.php](https://www.temis.nl/emissions/region_europe/datapage_nox.php).  
474 The European emissions data sets for countries NEC, LRTAP and large facilities E-PRTR are available  
475 on the website <https://www.eea.europa.eu/en/analysis/> of the EEA.  
476 The CAMS databases CAMS-REG-ANT v5.1 and CAMS-GLOB-TEMPO v3.1 are available on the ECCAD  
477 website on respectively <https://eccad.sedoo.fr/#/metadata/608/> and.  
478 <https://eccad.sedoo.fr/#/metadata/504/> (DOI:10.24380/ks45-9147).

479

#### 480 **Author contributions**

481 RA and JD made the improvements to DECSO, HE developed the superobservation code. RA  
482 did the processing, visualisations and main writing. JD and HE reviewed and edited the  
483 manuscript.

484

#### 485 **Competing interests**

486 The authors declare that they have no conflict of interest.

487

#### 488 **Acknowledgments**

489 This research was part of the Sentinel EO-based Emission and Deposition Service (SEEDS,  
490 Grant ID 101004318) project that has received funding from the European Union's Horizon  
491 2020 research and innovation programme. Sentinel-5 Precursor is a European Space Agency  
492 (ESA) mission on behalf of the European Commission. The TROPOMI payload is a joint  
493 development by ESA and the Netherlands Space Office. The Sentinel-5 Precursor ground  
494 segment development has been funded by ESA and with national contributions from the  
495 Netherlands, Germany, and Belgium. This work contains modified Copernicus Sentinel-5P  
496 TROPOMI data (2018–2023), processed locally at KNMI.

497

498

499

#### 500 **References**

501 Bayley, G. V., & Hammersley, J. M. (1946). The “Effective” Number of Independent Observations in an  
502 Autocorrelated Time Series. Supplement to the Journal of the Royal Statistical Society, 8(2), 184-197,  
503 <https://doi.org/10.2307/2983560>

504 Beirle, S., Borger, C., Dörner, S., Eskes, H., Kumar, V., de Laat, A., and Wagner, T.: Catalog of NO<sub>x</sub> emissions from  
505 point sources as derived from the divergence of the NO<sub>2</sub> flux for TROPOMI, Earth Syst. Sci. Data, 13, 2995-3012,  
506 <https://doi.org/10.5194/essd-13-2995-2021>, 2021.

507 Beirle, S., Borger, C., Jost, A., and Wagner, T.: Improved catalog of NO<sub>x</sub> point source emissions (version 2), Earth  
508 Syst. Sci. Data, 15, 3051–3073, <https://doi.org/10.5194/essd-15-3051-2023>, 2023.

509 Box, Jenkins, Reinsel, Time Series Analysis: Forecasting and Control, 4th Ed. Wiley (2008), ISBN 978-0-470-  
510 27284-8, p.30.

511 Božnar, M.Z., Mlakar, P., Grašič, B. and Tinarelli, G. (2012), Environmental impact assessment of a new thermal  
512 power plant Šoštanj Block 6 in highly complex terrain, Int. J. Environment and Pollution, Vol. 48, Nos. 1/2/3/4,  
513 pp.136–144.

514 Buchhorn, M. ; Smets, B. ; Bertels, L. ; De Roo, B. ; Lesiv, M. ; Tsendbazar, N. - E. ; Herold, M. ; Fritz, S,  
515 Copernicus Global Land Service: Land Cover 100m: collection 3: epoch 2019: Globe, 2020, DOI:  
516 10.5281/zenodo.3939050

517 Crippa, M., Guizzardi, D., Butler, T., Keating, T., Wu, R., Kaminski, J., Kuenen, J., Kurokawa, J., Chatani, S.,  
518 Morikawa, T., Pouliot, G., Racine, J., Moran, M. D., Klimont, Z., Manseau, P. M., Mashayekhi, R., Henderson, B.  
519 H., Smith, S. J., Suchyta, H., . . . Foley, K. (2023). The HTAP\_v3 emission mosaic: merging regional and global  
520 monthly emissions (2000–2018) to support air quality modelling and policies. Earth Syst. Sci. Data, 15(6), 2667-  
521 2694. <https://doi.org/10.5194/essd-15-2667-2023>

522 Ding, J., Miyazaki, K., van der A, R.J., Mijling, B., Kurokawa, J., Cho, S., Janssens-Maenhout, G., Zhang, Q., Liu, F.,  
523 and Levelt, P.F., Intercomparison of NO<sub>x</sub> emission inventories over East Asia, Atm. Chem. Phys., 2017a, 17,  
524 10125-10141, [doi.org/10.5194/acp-17-10125-2017](https://doi.org/10.5194/acp-17-10125-2017)

525 Ding, J., R.J. van der A, B. Mijling and P.F. Levelt, Space-based NO<sub>x</sub> emission estimates over remote regions  
526 improved in DECSO, Atmospheric Measurement Techniques, 2017b, 10, 925-938, doi:10.5194/amt-10-925-  
527 2017.

528 Ding, J., van der A, R. J., Eskes, H. J., Mijling, B., Stavrakou, T., van Geffen, J. H. G. M., Veefkind, J.P., NO<sub>x</sub>  
529 emissions reduction and rebound in China due to the COVID-19 crisis, Geophysical Research Letters, 46,  
530 e2020GL089912. <https://doi.org/10.1029/2020GL089912>, 2020.

531 Ding et al., NH<sub>3</sub> emissions from CrIS observations using DECSO, in preparation, 2024

532 Douros, J., Eskes, H., van Geffen, J., Boersma, K. F., Compernelle, S., Pinardi, G., Blechschmidt, A.-M., Peuch, V.-  
533 H., Colette, A., and Veefkind, P.: Comparing Sentinel-5P TROPOMI NO<sub>2</sub> column observations with the CAMS

534 regional air quality ensemble, *Geosci. Model Dev.*, 16, 509–534, <https://doi.org/10.5194/gmd-16-509-2023>,  
535 2023.

536 EC-JRC/PBL, European Commission, Joint Research Centre (JRC)/Netherlands Environmental Assessment  
537 Agency (PBL): Emission Database for Global Atmospheric Research (EDGAR), release EDGAR version 4.2,  
538 available at: <http://edgar.jrc.ec.europa.eu/overview.php?v=42>, 2011.

539 EPRT: European Pollutant Transfer Register, database version v4.2, available at: <http://prtr.ec.europa.eu/> (last  
540 access: 5 September 2023), 2012.

541 Fioletov, V., McLinden, C. A., Griffin, D., Krotkov, N., Liu, F., and Eskes, H.: Quantifying urban, industrial, and  
542 background changes in NO<sub>2</sub> during the COVID-19 lockdown period based on TROPOMI satellite observations,  
543 *Atmos. Chem. Phys.*, 22, 4201–4236, <https://doi.org/10.5194/acp-22-4201-2022>, 2022.

544 Fortems-Cheiney, A., Broquet, G., Pison, I., Saunois, M., Potier, E., Berchet, A., et al. (2021). Analysis of the  
545 anthropogenic and biogenic NO<sub>x</sub> emissions over 2008–2017: Assessment of the trends in the 30 most  
546 populated urban areas in Europe. *Geophysical Research Letters*, 48, e2020GL092206.  
547 <https://doi.org/10.1029/2020GL092206>

548 Guevara, M., Jorba, O., Tena, C., Denier van der Gon, H., Kuenen, J., Elguindi, N., Darras, S., Granier, C., and  
549 Pérez García-Pando, C.: Copernicus Atmosphere Monitoring Service TEMPORal profiles (CAMs-TEMPO): global  
550 and European emission temporal profile maps for atmospheric chemistry modelling, *Earth Syst. Sci. Data*, 13,  
551 367–404, <https://doi.org/10.5194/essd-13-367-2021>, 2021.

552 Guevara, M., Enciso, S., Tena, C., Jorba, O., Dellaert, S., Denier van der Gon, H., and Pérez García-Pando, C.: A  
553 global catalogue of CO<sub>2</sub> emissions and co-emitted species from power plants at a very high spatial and  
554 temporal resolution, *Earth Syst. Sci. Data Discuss.* [preprint], <https://doi.org/10.5194/essd-2023-95>, in review,  
555 2023.

556 Godłowska, J., M. J. Hajto, B. Lapeta, K. Kaszowski, The attempt to estimate annual variability of NO<sub>x</sub> emission  
557 in Poland using Sentinel-5P/TROPOMI data, *Atmospheric Environment*, Vol. 294, 2023, 119482,  
558 <https://doi.org/10.1016/j.atmosenv.2022.119482>.

559 Inness, A., Ades, M., Agustí-Panareda, A., Barré, J., Benedictow, A., Blechschmidt, A.-M., Dominguez, J. J.,  
560 Engelen, R., Eskes, H., Flemming, J., Huijnen, V., Jones, L., Kipling, Z., Massart, S., Parrington, M., Peuch, V.-H.,  
561 Razinger, M., Remy, S., Schulz, M., and Suttie, M.: The CAMS reanalysis of atmospheric composition, *Atmos.*  
562 *Chem. Phys.*, 19, 3515–3556, <https://doi.org/10.5194/acp-19-3515-2019>, 2019.

563 Janssens-Maenhout, G., Crippa, M., Guizzardi, D., Dentener, F., Muntean, M., Pouliot, G., Keating, T., Zhang, Q.,  
564 Kurokawa, J., Wankmüller, R., Denier van der Gon, H., Kuenen, J. J. P., Klimont, Z., Frost, G., Darras, S., Koffi, B.,  
565 and Li, M. HTAP\_v2.2: a mosaic of regional and global emission grid maps for 2008 and 2010 to study  
566 hemispheric transport of air pollution *Atmos. Chem. Phys.* 15, 11411-11432, 2015

567 Keppens, A. and Lambert, J.-C. (editors), Quarterly Validation Report of the Copernicus Sentinel-5 Precursor  
568 Operational Data Products #19: April 2018 – May 2023, S5P-MPC-IASB-ROCVR-19.01.00-20230703, version  
569 19.01.00 3 July 2023, (available at <https://mpc-vdaf.tropomi.eu/>).

570 Kostakis, G., Characterization of the fly ashes from the lignite burning power plants of northern Greece based  
571 on their quantitative mineralogical composition, *Journal of Hazardous Materials*, Vol. 166, 2009, Pages 972-  
572 977, <https://doi.org/10.1016/j.jhazmat.2008.12.007>.

573 Kubik, M.L., P.J. Coker, C. Hunt, The role of conventional generation in managing variability, *Energy Policy*, Vol.  
574 50, 2012, Pages 253-261, <https://doi.org/10.1016/j.enpol.2012.07.010>.

575 Kuenen, J., Dellaert, S., Visschedijk, A., Jalkanen, J.-P., Super, I., and Denier van der Gon, H.: CAMS-REG-v4: a  
576 state-of-the-art high-resolution European emission inventory for air quality modelling, *Earth Syst. Sci. Data*, 14,  
577 491–515, <https://doi.org/10.5194/essd-14-491-2022>, 2022.

578 Lin, X., R. J. van der A, J. de Laat, V. Huijnen, B. Mijling, J. Ding, H. Eskes, J. Douros, M. Liu, X. Zhang, Z. Liu,  
579 European soil NO<sub>x</sub> emissions derived from satellite NO<sub>2</sub> observations. *ESS Open Archive* . December 10, 2023.

580 Menut, L., Bessagnet, B., Khvorostyanov, D., Beekmann, M., Blond, N., Colette, A., Coll, I., Curci, G., Foret, G.,  
581 Hodzic, A., Mailler, S., Meleux, F., Monge, J.-L., Pison, I., Siour, G., Turquety, S., Valari, M., Vautard, R., and  
582 Vivanco, M. G.: CHIMERE 2013: a model for regional atmospheric composition modelling, *Geosci. Model Dev.*,  
583 6, 981–1028, <https://doi.org/10.5194/gmd-6-981-2013>, 2013.

584 Menut, L., B. Bessagnet, R. Briant, A. Cholakian, F. Couvidat, S. Mailler, R. Pennel, G. Siour, P. Tuccella, S.  
585 Turquety, and M. Valari. 2021. 'The CHIMERE v2020r1 online chemistry-transport model', *Geosci. Model Dev.*,  
586 14: 6781-811.

587 Miyazaki, K., Eskes, H., Sudo, K., Boersma, K. F., Bowman, K., and Kanaya, Y.: Decadal changes in global surface  
588 NO<sub>x</sub> emissions from multi-constituent satellite data assimilation, *Atmos. Chem. Phys.*, 17, 807-837,  
589 doi:10.5194/acp-17-807-2017, 2017.

590 Mijling, B. and R.J. van der A, Using daily satellite observations to estimate emissions of short-lived air  
591 pollutants on a mesoscopic scale, *J. Geophys. Res.*, 117, 2012, doi:10.1029/2012JD017817

592 Mijling et al., in preparation, 2024

593 Pinterits, M., B. Ullrich, T. Bartmann and M. Gager, European Union emission inventory report 1990-2019  
594 under the UNECE Convention on Long-range Transboundary Air Pollution (Air Convention), EEA Report No  
595 5/2021, 2021NEC, Air pollution in Europe: 2023 reporting status under the National Emission reduction  
596 Commitments Directive, 2023 ([https://www.eea.europa.eu/publications/national-emission-reduction-  
597 commitments-directive-2023/air-pollution-in-europe-2023](https://www.eea.europa.eu/publications/national-emission-reduction-commitments-directive-2023/air-pollution-in-europe-2023))

598 Quitzow, R., G. Bersalli, L. Eicke, J. Jahn, J. Lilliestam, F. Lira, A. Marian, D. Süsner, S. Thapar, S. Weko, S. Williams,  
599 B. Xue, The COVID-19 crisis deepens the gulf between leaders and laggards in the global energy transition,  
600 *Energy Research & Social Science*, Vol. 74, 2021, 101981, <https://doi.org/10.1016/j.erss.2021.101981>.

601 Rijsdijk, P., H.J. Eskes, A. Dingmans, K.F. Boersma, T. Sekiya, K. Miyazaki, and S. Houweling, Constructing  
602 superobservations from satellite NO<sub>2</sub> for assimilation and model evaluation, preprint 2024.

603 Sekiya, T., Miyazaki, K., Eskes, H., Sudo, K., Takigawa, M., and Kanaya, Y.: A comparison of the impact of  
604 TROPOMI and OMI tropospheric NO<sub>2</sub> on global chemical data assimilation, *Atmos. Meas. Tech.*, 15, 1703–  
605 1728, <https://doi.org/10.5194/amt-15-1703-2022>, 2022.

606 Shindell, D. T., Faluvegi, G., Bell, N., and Schmidt, G. A. (2005), An emissions-based view of climate forcing by  
607 methane and tropospheric ozone, *Geophys. Res. Lett.*, 32, L04803, doi:[10.1029/2004GL021900](https://doi.org/10.1029/2004GL021900)

608 Skoulidou, I.; Koukouli, M.-E.; Segers, A.; Manders, A.; Balis, D.; Stavrakou, T.; van Geffen, J.; Eskes, H. Changes  
609 in Power Plant NO<sub>x</sub> Emissions over Northwest Greece Using a Data Assimilation Technique. *Atmosphere* 2021,  
610 12, 900. <https://doi.org/10.3390/atmos12070900>

611 Streets, D.G., Canty T., Carmichael, G.R., de Foy B., Dickerson, R.R. Duncan, B.N., Edwards, D.P., Haynes, J.A.,  
612 Henze, D.K., Houyoux, M.R., Jacob, D.J., Krotkov, N.A., Lamsal, L.N., Liu, Y., Lu, Z., Martin, R.V., Pfister G.G.,  
613 Pinder R.W., Salawitch R.J., Wecht, K.J., Emissions estimation from satellite retrievals: A review of current  
614 capability, *Atmospheric Environment*, 77, 2013, 1011-1042, <https://doi.org/10.1016/j.atmosenv.2013.05.051>.

615 Thunis, P., M. Crippa, C. Cuvelier, D. Guizzardi, A. de Meij, G. Oreggioni, E. Pisoni, Sensitivity of air quality  
616 modelling to different emission inventories: A case study over Europe, *Atmospheric Environment: X*, Volume  
617 10, 2021, <https://doi.org/10.1016/j.aeaa.2021.100111>.

618 van der A, R.J., de Laat, A.T.J., Ding, J., Eskes, H.J., Connecting the dots: NO<sub>x</sub> emissions along a West Siberian  
619 natural gas pipeline, *npj Clim Atmos Sci* 3, 16, <https://doi.org/10.1038/s41612-020-0119-z>, 2020

620 van Geffen, J. H. G. M., Eskes, H. J., Compernelle, S., Pinardi, G., Verhoelst, T., Lambert, J.-C., Sneep, M., ter  
621 Linden, M., Ludewig, A., Boersma, K.F. and Veefkind, J.P.: Sentinel-5P TROPOMI NO<sub>2</sub> retrieval: impact of version  
622 v2.2 improvements and comparisons with OMI and ground-based data, *Atmos. Meas. Tech.*, 15, 2037-2060.  
623 <https://doi.org/10.5194/amt15-2037-2022>, 2022a.

624 van Geffen, J. H. G. M., Eskes, H. J., Boersma, K. F. and Veefkind, J. P.: TROPOMI ATBD of the total and  
625 tropospheric NO<sub>2</sub> data products, Report S5P-KNMI-L2-0005-RP, version 2.4.0, 202207-11, KNMI, De Bilt, The  
626 Netherlands, <http://www.tropomi.eu/data-products/nitrogen-dioxide/> (last access: 06 Dec. 2022), 2022b

627 Veefkind, J.P., Aben, I., McMullan, K., Förster, H., Vries, J., de Otter, G., Claas, J., Eskes, H.J., Haan, J.F. de,  
628 Kleipool, Q., Weele, M. van, Hasekamp, O., Hoogeveen, R., Landgraf, J., Snel, R., Tol, P., Ingmann, P., Voors, R.,  
629 Kruizinga, B., Vink, R., Visser, H., Levelt, P.F., 2012. TROPOMI on the ESA Sentinel-5 Precursor: a GMES mission  
630 for global observations of the atmospheric composition for climate, air quality and ozone layer applications.  
631 *Rem. Sens. Environ.* 120, 70–83. <https://doi.org/10.1016/j.rse.2011.09.027>.

632 Williams, J. E., Boersma, K. F., Le Sager, P., and Verstraeten, W. W.: The high-resolution version of TM5-MP for  
633 optimized satellite retrievals: description and validation, *Geosci. Model Dev.*, 10, 721–750,  
634 <https://doi.org/10.5194/gmd-10-721-2017>, 2017.

635 Zhang, X., van der A, R., Ding, J., Zhang, X., and Yin, Y., Significant contribution of inland ships to the total NO<sub>x</sub>  
636 emissions along the Yangtze River, *Atmos. Chem. Phys.*, 23, 5587–5604, [https://doi.org/10.5194/acp-23-5587-](https://doi.org/10.5194/acp-23-5587-2023)  
637 2023, 2023.  
638  
639